Advances in Engineering Software 182 (2023) 103478

Contents lists available at ScienceDirect

Advances in Engineering Software

journal homepage: www.elsevier.com/locate/advengsoft

Multi-resolution topology optimization using B-spline to represent the density field

Zhenbiao Guo [a], Hailiang Su [b], Xinqing Li [a], Yingjun Wang [a,c,*]

[a] National Engineering Research Center of Novel Equipment for Polymer Processing, The Key Laboratory of Polymer Processing Engineering of the Ministry of Education, Guangdong Provincial Key Laboratory of Technique and Equipment for Macromolecular Advanced Manufacturing, South China University of Technology, Guangzhou 510641, China

[b] School of Mechanical and Automotive Engineering, Guangxi University of Science and Technology, Liuzhou 545006, China

[c] State Key Laboratory of Digital Manufacturing Equipment and Technology, Huazhong University of Science and Technology, Wuhan 430074, China

ARTICLE INFO

Keywords:
Multi-resolution topology optimization
Computational efficiency
B-spline
Post-processing
Computer-aided design

ABSTRACT

This paper proposes a novel multi-resolution topology optimization method using B-spline to represent the density field, and overcomes the defects of tedious post-processing of element-based models and low computational efficiency of topology optimization for large-scale problems. The design domain embedded in the B-spline space is discretized with a coarser analysis mesh and a finer density mesh to reduce the computational cost of finite element analysis. As design variables, the coefficients of the control points control the shape of the B-spline. The optimized B-spline can be quickly and precisely converted into a CAD model. Sensitivity filtering is additionally applied to enhance B-spline's smoothness and suppress QR-patterns. Numerical examples, including 2D and 3D cases, are tested to demonstrate that the proposed method significantly saves computational time without sacrificing the performance of the optimized structure. Moreover, the post-processing procedures are streamlined, resulting in continuous, smooth, and editable models.

1. Introduction

As an optimization technique, topology optimization (TO) can automatically search the optimal distribution of materials in a design domain to produce a high-performance structure. Currently, with the enormous demand for practical engineering, TO is extensively implemented in mechanical [1–3], fluid [4,5], thermal [6–8], electromagnetic [9,10], acoustic [11,12], nonlinear material [13,14], multi-material [15–17] and multi-scale problems [18–20] due to the high degree of design freedom and the low dependence on expert experience it offers. Simultaneously, several important TO methods have been developed, including the homogenization method [21], the solid isotropic material with penalization (SIMP) method [22,23], the evolutionary structural optimization (ESO) [24,25], the level-set method (LSM) [26–28], and the movable morphable components (MMC) method [29,30]. Among them, the density-based SIMP method, which is simple and versatile, has become the most commonly used TO method. However, SIMP presently faces challenges with the tedious post-processing of element-based models and the low computational efficiency of large-scale problems.

Generally, the optimized element-based model should be converted into the computer-aided design (CAD) model in post-processing. However, "zigzag" boundaries and some elements with intermediate densities of the element-based model bring plenty of troubles to CAD modeling. The general boundary reconstruction of a 3D element-based model is to seek a number of contour points to form the structure surface, resulting in a CAD model represented by triangular patches [31]. These triangular patches are typically not smooth, so the subsequent geometric fitting relies on tedious manual adjustment. In order to simplify the post-processing and prevent manual tasks, the B-spline, which frequently occurs in CAD environments, is adopted by researchers to represent the structure in TO. Eschenauer et al. [32] proposed the "bubble method", which changes the distribution of materials by introducing holes (i.e., bubbles) into the design domain and moving the boundaries. B-splines represents the bubbles and the outermost boundary, and the design variables are the location of the control points. Seo et al. [33] used a non-uniform rational B-spline (NURBS) plane and trimming curves to create trimmed spline surfaces, and the control points are moved to change the shape of the trimmed spline surfaces. Remarkably, this work is the first application of isogeometric analysis (IGA) to TO. Hassani et al. [34] employed the NURBS function to

* Corresponding author.
E-mail address: wangyj84@scut.edu.cn (Y. Wang).

https://doi.org/10.1016/j.advengsoft.2023.103478
Received 1 December 2022; Received in revised form 24 February 2023; Accepted 17 April 2023
Available online 26 April 2023

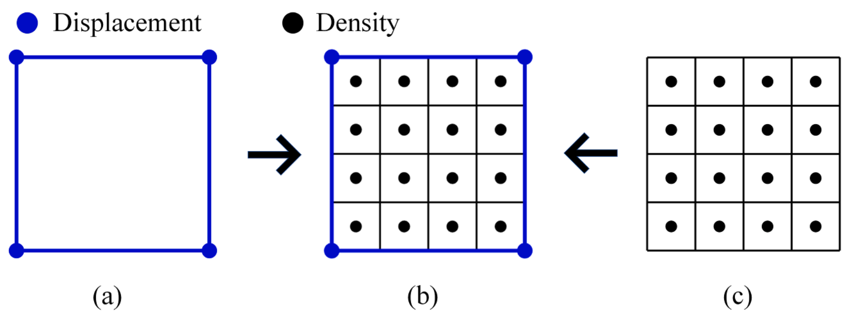

Fig. 1. Elements in MTOP: (a) analysis element, (b) superposed element, (c) 4 × 4 density elements.

represent the density field of the design domain and performed IGA to optimize the NURBS shape. Gao et al. [35] constructed a more continuous and smoother density field by utilizing the NURBS function and the Shepard function, where IGA is also exploited to address the structure response. Despite certain advantages of IGA, traditional finite element analysis (FEA) remains the most attractive analytical method in TO because it can handle complex engineering problems using commercial FEA software. Qian [36] presented a new form of density based TO where a B-spline function is employed to represent the density field, and the design domain is discretized via linear elements. Subsequently, Costa et al. [37,38] furnished a research idea, namely the NURBS-based SIMP method, which constructs 2D/3D density fields utilizing NURBS surfaces/hyper-surfaces, respectively. Since B-spline is compatible with CAD, converting surfaces/hyper-surfaces based on it to CAD models is quick and accurate [39].

Nevertheless, a relatively evident problem with the FEA method is that when dealing with large-scale TO problems, since the design domain must be discretized into a great number of elements, the analysis part requires considerable computation and thus consumes substantial computational time in each iteration. The adaptive meshing methods [40–44] can noticeably alleviate the computational burden of FEA by cutting down the number of elements. In these works, elements of different sizes are used adaptively at different locations in the design domain. Additionally, graphics processing unit (GPU) parallel computing [45–50] is applied to improve the computational efficiency of TO by multithreading computing tasks. Fast solvers [51,52] and approximate reanalysis [53,54] are as well valuable methods to improve the efficiency of TO. By contrast, Nguyen et al. [55,56] provided a new research idea that utilizes a coarser analysis mesh to perform the FEA and a finer density mesh to represent the topology, known as multi-resolution topology optimization (MTOP). Consequently, the computational cost of the FEA is significantly reduced while obtaining the high-resolution structure. MTOP has been adopted to promote the computational efficiency of the MMC method [57], where the FEA and geometric models are also decoupled. Besides, MTOP is also broadly applied to tackle complex TO problems such as multi-material [58,59], uncertainty [60], and geometric nonlinearity [61]. It is noteworthy that there is an upper limit on the number of density elements in an analysis element for a given order of shape function and filter radius. Exceeding this limit can overestimate the analysis element's stiffness and lead to numerical artifacts of material discontinuities (i.e., QR-patterns) [62]. Although high-order finite elements can be availed to suppress the QR-patterns [63–66], the computational time increases.

This paper proposes a novel method called multi-resolution topology optimization using B-spline (MTOBS) to reduce the computational cost and simultaneously simplify the post-processing procedure. The design domain is discretized through a coarser analysis mesh and a finer density mesh aiming to reduce computational time in FEA. A bivariate B-spline function (i.e., B-spline surface) is employed to represent the density field for the 2D design domain, and a trivariate B-spline function (i.e., B-spline hyper-surface) to represent the density field for 3D design domain. The coefficients of the control points are set as the design variables to govern the shape of the B-spline. Due to the continuity and CAD compatibility of B-splines, the surface/hyper-surface based on it can be quickly and precisely converted into a CAD model in post-processing. In addition, sensitivity filtering [67,68] is used to improve the smoothness of the B-spline and suppress QR-patterns. MTOBS optimizes the integrated process from TO to CAD, resulting in continuous, smooth, and editable models.

The remainder of this paper is organized as follows. The underlying concept and formulation of MTOP are presented in Section 2. Section 3 describes the theoretical implementation of MTOBS. Section 4 introduces the integrated process from the practical implementation of MTOBS to the post-processing of CAD modeling. Numerical examples are presented, and the results are discussed in Section 5. Finally, the conclusion is given in Section 6.

2. Concept of multi-resolution topology optimization (MTOP)

2.1. The SIMP method

The MTOP method is developed based on the SIMP method. As one of the most important TO methods, the SIMP method discretizes the design domain into a finite number of elements and assigns each element a relative density between 0 and 1. The relative elemental densities are iteratively updated as design variables toward 0 or 1 according to the sensitivity information. A penalty factor is used to interpolate the Young's modulus of the elements for FEA. Based on the modified SIMP method [69], the Young's modulus of the element is defined as follows:

$$E_e(\rho_e) = E_{\min} + (E_0 - E_{\min})(\rho_e)^s \tag{1}$$

where ρ_e is the density of the element *e;* E_0 is the original Young's modulus; $E_{\min}$ is the minimum value of the Young's modulus of the material to avoid singularity; and s is referred to as the penalty factor typically set to 3. A typical optimization objective is to keep a certain volume fraction of the structure while minimizing the compliance. The optimization problem can be stated mathematically as follows:

$$\begin{aligned}
&\text{find}: && \boldsymbol{\rho} = [\rho_1, \rho_2, \ldots, \rho_n]^{\mathrm{T}} \\
&\text{min}: && c = \boldsymbol{U}^{\mathrm{T}}\boldsymbol{K}\boldsymbol{U} = \sum_{e=1}^{n} (\boldsymbol{u}_e)^{\mathrm{T}}\boldsymbol{k}_e\boldsymbol{u}_e = \sum_{e=1}^{n} E_e(\rho_e)(\boldsymbol{u}_e)^{\mathrm{T}}\boldsymbol{k}_0\boldsymbol{u}_e \\
&\text{subject to.}: && \boldsymbol{K}\boldsymbol{U} = \boldsymbol{F} \\
&&& g = \sum_{e=1}^{n} \rho_e v_e - V_{\max} \le 0 \\
&0 \le \rho_e \le 1, e = 1, 2, \ldots, n
\end{aligned} \tag{2}$$

where $\boldsymbol{\rho}$ is the element density vector; n is the total number of elements in the design domain; c is the compliance; $\boldsymbol{U}$ is the global displacement vector; $\boldsymbol{K}$ is the global stiffness matrix; $\boldsymbol{u}_e$ is the element displacement vector; $\boldsymbol{k}_e$ is the element stiffness matrix; $\boldsymbol{k}_0$ is the element stiffness matrix for an element with unit Young's modulus; $\boldsymbol{F}$ is the load vector; g is the volume constraint; v_e is the element volume; $V_{\max}$ is the target volume.

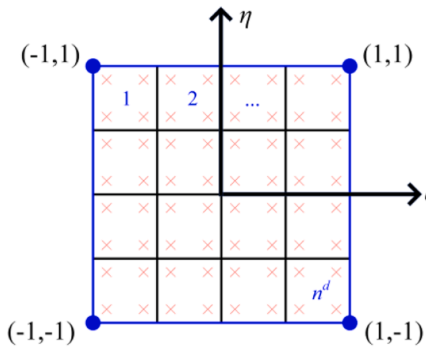

Fig. 2. Analysis element in the natural coordinate system and Gauss integration points (red cross).

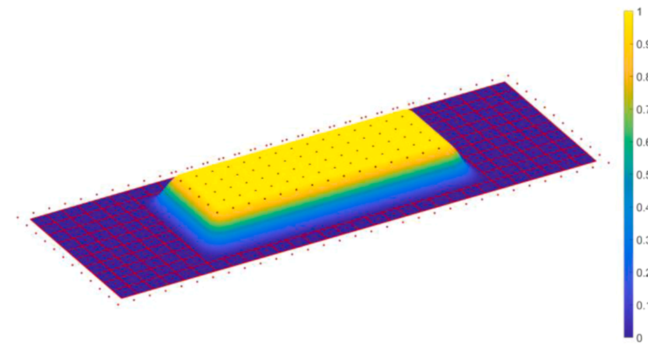

Fig. 3. B-spline surface, control points (red points), and effective knot spans (red squares).

2.2. The MTOP method

In the SIMP method, the mesh for FEA and the density mesh are coupled. The design domain is discretized with more density elements in large-scale optimization problems, which significantly raises the computational cost of FEA. In contrast, MTOP [55] decouples the analysis mesh from the density mesh, using a coarser analysis mesh to perform FEA. The structure obtained from MTOP on a coarse analysis mesh has the exact resolution as that obtained from SIMP on a fine analysis mesh. The difference is that MTOP requires less computational cost. The analysis element in MTOP is generally the quadrilateral element for 2D analysis or the hexahedral element for 3D analysis, and an analysis element contains n^d density elements inside. n is the number of density elements in one direction and d is the dimension of the element. Unless otherwise specified, all analysis elements in this paper include four density elements in one direction. As Fig. 1 shows, a 2D analysis element contains 4 × 4 density elements.

Although the density in the density element is element-wise constant, the density in the analysis element is non-uniform because each density element has a different density. The main idea of calculating the analysis element's stiffness matrix is to divide it into several density elements regions, and integrate the regions separately with Gauss integration to obtain the unit stiffness matrix components of density elements, and then add them up. Unless otherwise stated, we set 2 × 2 Gauss integration points in each 2D density element and 2 × 2 × 2 in each 3D density element to calculate the unit stiffness matrix component. The main reason is that the FEA process of using coarse analysis mesh is essentially low precision, and the second-order Gaussian integration is sufficient to meet the precision requirements.

As shown in Fig. 2, the stiffness matrix of a 2D analysis element, which has been mapped into the natural coordinate system ranging from −1 to 1, is calculated as follows:

$$\begin{aligned} \boldsymbol{k}_e &= \int_{-1}^{1}\int_{-1}^{1} \boldsymbol{B}^{\mathrm{T}}\boldsymbol{D}\boldsymbol{B}|\boldsymbol{J}|d\xi d\eta \\ &= \frac{A_e}{4}\sum_{i=1}^{n^d}\left(E_i(\rho_i)\sum_{g=1}^{n_i}\theta_{ig}\boldsymbol{B}(\xi_{ig},\eta_{ig})^{\mathrm{T}}\boldsymbol{D}_0\boldsymbol{B}(\xi_{ig},\eta_{ig})\right) \end{aligned} \tag{3}$$

where $\boldsymbol{B}$ is the strain-displacement matrix; $\boldsymbol{D}$ is the constitutive matrix; $\boldsymbol{J}$ is the Jacobi matrix; A_e is the volume of the analysis element; n^d represents the number of density elements in one analysis element; ρ_i is the density value of the density element; n_i is the number of Gauss integration points in a density element; θ_{ig} and (ξ_{ig}, η_{ig}) denotes the weight and coordinate of the Gauss integration point, respectively; $\boldsymbol{D}_0$ is the constitutive matrix with unit Young's modulus. During iterations, the stiffness matrix of the analysis element is computed based on the density values of the density elements and the corresponding unit stiffness matrix components. Since the unit stiffness matrix components of density elements at the same position are identical for different analysis elements, only n^d unit stiffness matrix components need to be computed and stored before the iterations.

3. Multi-resolution topology optimization using B-spline (MTOBS)

3.1. B-spline function

Currently, B-spline and NURBS [70] are the standard representations in CAD systems. A univariate B-spline function of degree p is defined as follows:

$$f(\xi) = \sum_{i=0}^{n}\omega_i B_{i,p}(\xi) \tag{4}$$

where ω_i is referred to as the coefficient of control points; $B_{i,p}(\xi)$ represents the B-spline basis function, defined on a knot vector $\Xi = \{\xi_1, \xi_2, \ldots, \xi_{n+p+1}\}$. The uniform B-spline, which means that the knot spans of the knot vector Ξ are uniform, is employed in this paper. A B-spline basis function of degree p is defined recursively as follows:

$$\begin{aligned} B_{i,p}(\xi) &= \frac{(\xi-\xi_i)B_{i,p-1}(\xi)}{\xi_{i+p}-\xi_i} + \frac{(\xi_{i+p+1}-\xi)B_{i+1,p-1}(\xi)}{\xi_{i+p+1}-\xi_{i+1}} \\ B_{i,0}(\xi) &= \begin{cases} 1, \xi_i \le \xi \le \xi_{i+1} \\ 0, \mathit{Otherwise} \end{cases} \end{aligned} \tag{5}$$

Correspondingly, the bivariate B-spline function (i.e., B-spline surface) of degree p in ξ direction and degree q in η direction can be expressed as follows:

$$f(\xi,\eta) = \sum_{k=0}^{n}\sum_{l=0}^{m}B_{k,p}(\xi)B_{l,q}(\eta)\omega_{k,l} = \sum_{r=0}^{(m+1)(n+1)}N_r(\xi,\eta)\omega_r \tag{6}$$

where $N_r(\xi, \eta)$ is the basis function of the bivariate B-spline in the form of a tensor product. To facilitate understanding, Fig. 3 displays a B-spline surface of degree 2 both in ξ direction and η direction, where the number of control points and the effective knot spans size are 32 × 12 and 30 × 10, respectively. Moreover, the coefficients of the middlemost 16 × 6 control points are set to 1, and the coefficients of other control points are set to 0.

3.2. MTOBS and sensitivity analysis

To improve the efficiency of large-scale topology optimization problems and overcome the defects of tedious post-processing of element-based models, this paper proposes a novel multi-resolution topology optimization method using B-spline to represent the density field (MTOBS). The design domain is discretized through a coarse analysis mesh and a fine density mesh. The coarse analysis mesh is utilized to

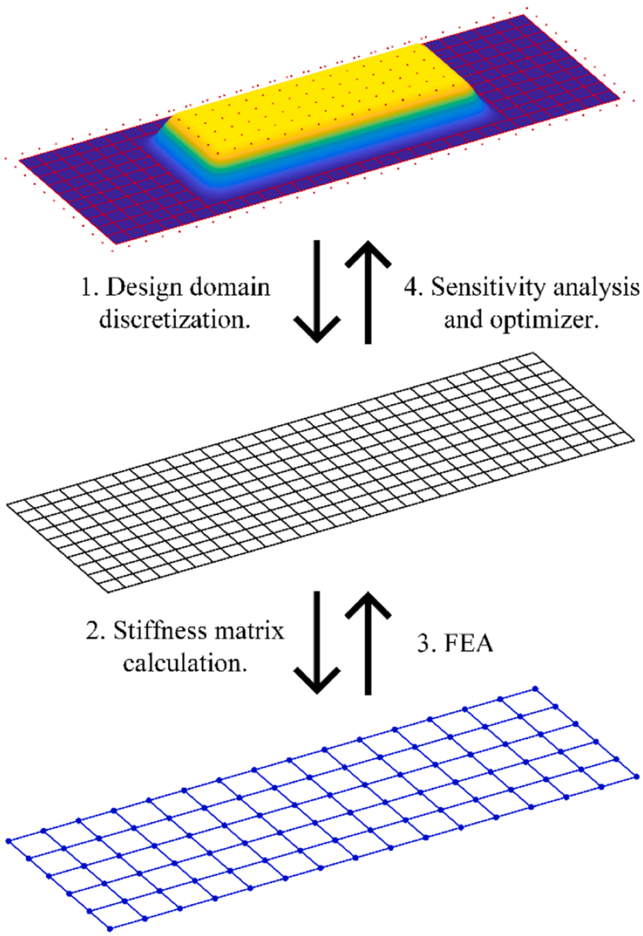

Fig. 4. The structure and process of MTOBS: B-spline surface (top surface), density mesh (middle squares), and analysis mesh (bottom squares).

perform the FEA with low computational cost and the fine density mesh allows us to obtain a smooth and continuous B-spline. For a 2D problem, a bivariate B-spline function (i.e., B-spline surface) is used to represent the density field, and the design domain is embedded in this surface's projection area on the horizontal plane. Note that the design domain should be smaller than or coincide with the area of effective knot spans. The density value of the design domain is reflected by the B-spline function value, i.e., the height of the surface in the vertical direction. Similarly, for a 3D problem, a trivariate B-spline function (i.e., B-spline hyper-surface) is adopted to characterize the density field. The design domain is embedded into the hyper-surface's 3D projection region, and the height in the fourth dimension can represent the density value. As the design variables, the coefficients of control points control the shape of the B-spline.

Here, Fig. 4 is taken to further illustrate the structure and process of the developed MTOBS. Firstly, the B-spline surface is constructed to represent the density field, and the design domain is divided into a coarser analysis mesh and a finer density mesh. The density values of the density elements are calculated according to the position of their center point in the density field. Secondly, the stiffness matrixes of the analysis elements are calculated according to the density values of the density elements. Thirdly, the FEA equations are solved based on the analysis mesh to obtain the structural responses. Finally, the sensitivities of the objective function to the design variables are calculated according to the chain rule, and the design variables are updated by the optimizer. The optimized design variables are used for the next cycle until convergence.

The density value in each density element is element-wise constant and is calculated according to the location of its center point in the design domain by a bivariate or trivariate B-spline function. In the proposed MTOBS, all analysis is done with quadrilateral four-node (Q4) linear elements for 2D problems or hexahedral eight-node (Q8) linear elements for 3D problems. The sensitivity analysis formula in 2D cases is derived below, and the formula in 3D cases is similar. For 2D problems, according to the stiffness matrix of the analysis element derived from Eq. (3), the sensitivity of the compliance to the density value is given by:

$$\frac{\partial c}{\partial \rho_i} = -s(\rho_i)^{s-1}(E_0 - E_{\min})\frac{A_e}{4}\sum_{g=1}^{n_i}\theta_{ig}\boldsymbol{B}(\xi_{ig},\eta_{ig})^{\mathrm{T}}\boldsymbol{D}_0\boldsymbol{B}(\xi_{ig},\eta_{ig}) \tag{7}$$

where ρ_i is the density value derived from Eq. (6) by its center point coordinates (ξ_i, η_i). However, since the design variables are the coefficients of the B-spline control points rather than the density values, the sensitivity of the objective function to the design variable is modified in terms of the chain rule as follows:

$$\frac{\partial c}{\partial \omega_r} = \sum_{i\in\Omega_r}\frac{\partial c}{\partial \rho_i}\frac{\partial \rho_i}{\partial \omega_r} = \sum_{i\in\Omega_r}\frac{\partial c}{\partial \rho_i}N_r(\xi_i,\eta_i) \tag{8}$$

where Ω_r represents a set of density elements whose center point falls in the knot spans spanned by the B-spline basis function of the control point ω_r. The sensitivity of the volume constraint to the density value is given by:

$$\frac{\partial g}{\partial \rho_i} = v_i \tag{9}$$

where v_i is the volume of the density element. The sensitivity of the volume constraint to the design variables is formulated similarly according to the chain rule as follows:

$$\frac{\partial g}{\partial \omega_r} = \sum_{i\in\Omega_r}\frac{\partial g}{\partial \rho_i}\frac{\partial \rho_i}{\partial \omega_r} = \sum_{i\in\Omega_r}v_iN_r(\xi_i,\eta_i) \tag{10}$$

3.3. Filters in MTOBS

In the developed MTOBS, we utilize both the inherent filtering provided by the B-spline [36,71] and the traditional sensitivity filter. As an essential property of B-spline, the local support means that a B-spline basis function spans $(p+1)\times(q+1)$ knot spans. In other words, there are $(p+1)\times(q+1)$ non-zero basis functions in an effective knot span. This property brings an implicit filtering effect to TO when the density field is represented by the B-spline function. The filtering range size relies on the B-spline degree and the knot span size. Besides, the storage cost of the implicit filter is linear since there is no requirement to store information of surrounding elements.

In order to enhance the smoothness of the B-spline and further control the filter range, the traditional sensitivity filter is additionally employed in this paper. Compared to the density filter, the sensitivity filter is less frequently used in TO. We choose the sensitivity filter for two reasons. Firstly, the sensitivity filter has lower computation and storage costs because it directly deals with the partial derivatives of the objective function to the design variables, while the density filter operates on the density values of the density elements. In MTOBS, the design variables are the B-spline control point coefficients, with a lower number than density elements. Secondly, even if we use the density filter on control point density, optimization results are worse than the sensitivity filter due to error from the sensitivity correction based on the distance function. The sensitivity of the objective function to the design variables is filtered before each update of design variables. The filtered sensitivity is given by:

$$\overline{\frac{\partial c}{\partial \omega_r}} = \frac{1}{\max(\gamma,\omega_r)\sum_{s\in\Omega_r}H_{rs}}\sum_{s\in\Omega_r}H_{rs}\omega_s\frac{\partial c}{\partial \omega_s} \tag{11}$$

where $\gamma(=10^{-3})$ is a minimal positive number used to prevent the

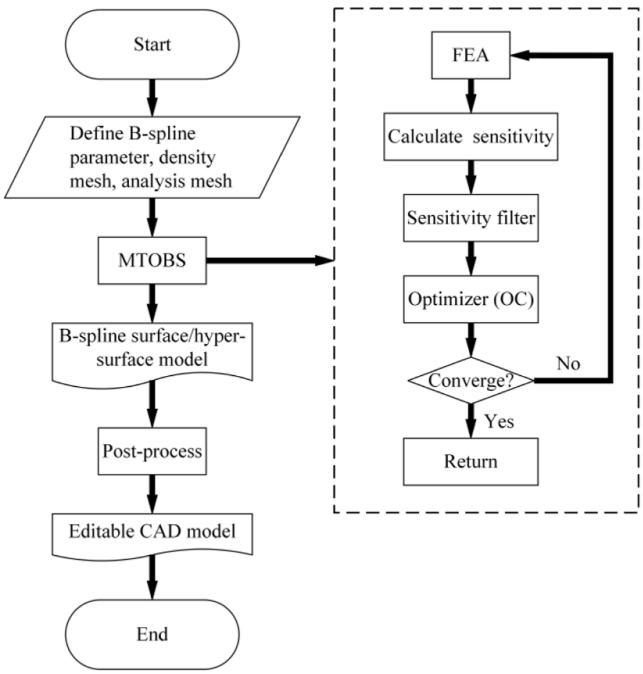

Fig. 5. The flowchart of the integrated process from optimization to design.

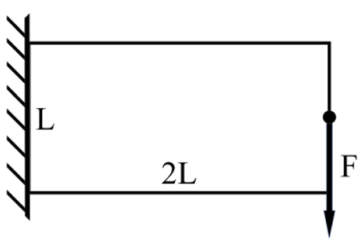

Fig. 6. A 2D cantilever diagram.

denominator from being 0; Ω_r is a set of control points ω_s whose distance Δ_{rs} from the control point ω_r is shorter than the filter radius $r_{\min}$; H_{rs} denotes weight factor, which is defined as:

$$H_{rs} = \max(0, r_{\min} - \Delta_{rs}) \tag{12}$$

Thus, in this work, there is not only the implicit filtering effect brought by the local support of B-spline but also the filtering effect of the sensitivity filter. The filtering range is governed by three parameters: the B-spline degree, the knot span size, and the filtering radius. With the proper choice of these three parameters, we are able to suppress the numerical artifacts, such as QR-patterns in MTOP, and control the minimal feature length.

4. Integrated process from optimization to design

In this section, with the aim of demonstrating the benefits of the developed MTOBS in post-processing design results, we apply two benchmark problems in TO, including 2D and 3D cantilever beams, to implement the integrated process from optimization (i.e., MTOBS) to design (i.e., CAD model). The optimality criterion (OC) method [72] is employed to update the design variables according to the sensitivity information. In addition to implementing MTOBS, the optimized B-spline surface/hyper-surface will be converted into an editable CAD model. The related post-processing operation is performed in the commercial CAD software Rhinoceros (Seattle, WA). The flowchart of the integrated process is depicted in Fig. 5.

4.1. 2D cantilever design

As shown in Fig. 6, the cantilever is fixed at the left edge, and a unit point load is applied downward at the midpoint of the right edge. The objective of the optimization is to minimize the structural compliance while keeping the volume fraction of the optimized structure to the original structure is 50%.

A bivariate B-spline function of degree 2 both in ξ and η direction is employed to represent the density field. The size of control points and effective knot spans are 82 × 42 and 80 × 40, respectively. The design domain coincides with the area of effective knot spans and is discretized into a density mesh size of 160 × 80 and an analysis mesh size of 40 × 20. The sensitivity filtering radius is set to 1.5 times the size of a knot span. The optimization results, including the optimized B-spline surface and the density mesh distribution, are shown in Fig. 7.

The B-spline surface can be directly converted into a CAD model in CAD software due to the CAD-compatibility of the B-spline. The post-processing procedure of the optimized B-spline surface shown in Fig. 7(a) is exhibited in Fig. 8. Firstly, the optimized B-spline surface is stored as an igs file, and the igs file is imported into the CAD software. Then, we can draw a plane in the horizontal plane slightly larger than the projection area of the B-spline surface and adjust the plane to the threshold height. The selection criterion for the threshold value is that the post-processed CAD model should satisfy the volume constraint. Next, the intersection tool is used to obtain the intersection line between the B-spline surface and the plane. The outer boundary lines also need to be added. Lastly, the solid area is filled to form the structure plane according to the boundary lines. The structure plane can be edited and stored as a new igs file. The gray feature of Fig. 7(b) will be kept if the B-spline surface corresponding to it is higher than the horizontal plane; otherwise, it will be eliminated. This method enables exact segmentation inside the elements and goes beyond simply preserving or eliminating the gray elements. Due to the continuity of the B-spline, the related operation of post-processing is almost error-free. So far, the integrated process of the 2D cantilever from MTOBS to an editable CAD model has been completed. Note that it is difficult to precisely accomplish the volume fraction desired by users by selecting the height of the threshold plane during post-processing of the optimized B-spline. We

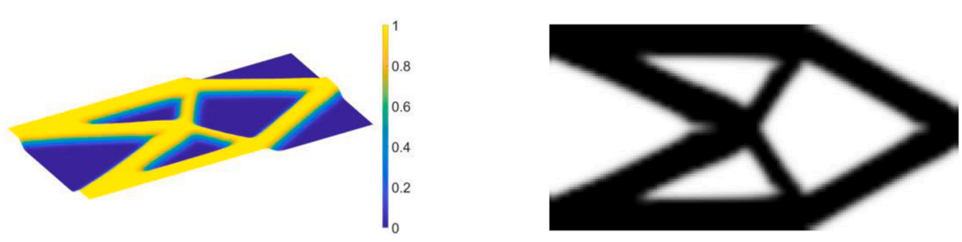

(a) (b)

Fig. 7. Optimization results for the 2D cantilever of MTOBS: (a) B-spline surface, (b) density mesh distribution.

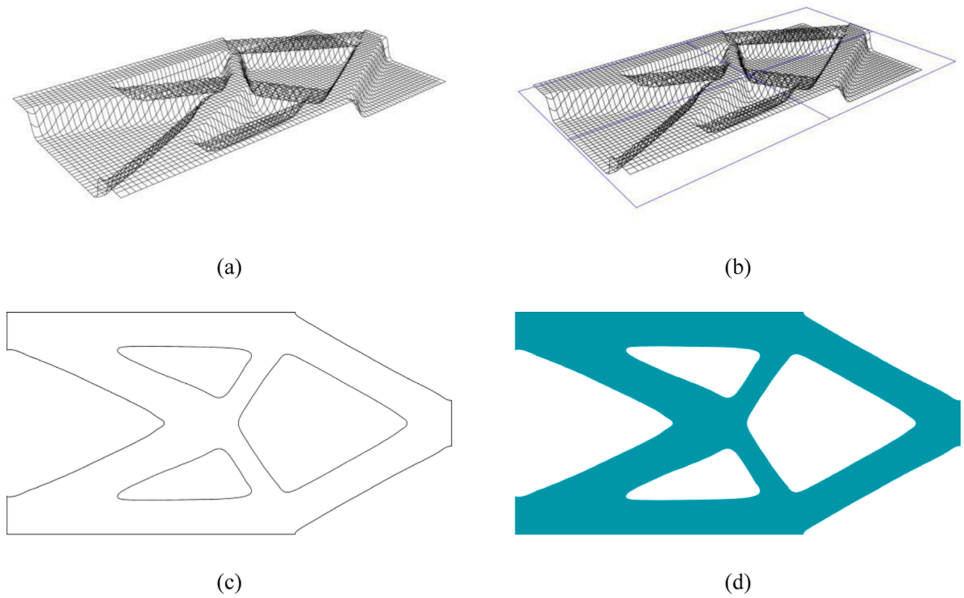

Fig. 8. The post-processing procedure of the optimized B-spline surface: (a) Import the igs file of the B-spline surface into the CAD software; (b) Draw a plane in the horizontal direction and adjust it to the threshold height; (c) Find the intersection line between the B-spline surface and the plane; (d) Fill the solid area to form the plane according to the boundary lines.

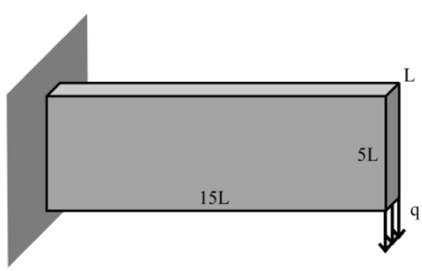

Fig. 9. A 3D cantilever diagram.

roughly get at the volume fraction using a trial-and-error approach. This trial-and-error process often takes two to three times, and the volume fraction cannot precisely meet the requirements. However, the model with approximate volume fraction is sufficient to meet the actual needs of the project, because the model's shape must still be modified to match actual engineering requirements.

4.2. 3D cantilever design

As a 3D cantilever shown in Fig. 9, the left side is fixed, and the unit uniform load is applied downward at the lower right edge. For compliance minimization with a volume fraction of 30%, a trivariate B-spline function of degree 2 in the ξ, η, and ζ directions is employed. The size of control points and effective knot spans are $62 \times 22 \times 6$ and $60 \times 20 \times 4$, respectively. A density mesh size of $120 \times 40 \times 8$ and an analysis mesh size of $30 \times 10 \times 2$ are employed to discretize the 3D design domain, which similarly coincides with the domain of the effective knot spans. The sensitivity filtering radius is 1.5 times the size of a knot span. Since the 4D optimized B-spline hyper-surface cannot be plotted in 3D space, it is depicted here by uniformly sampled points from itself for visualization. The color of each sampled point represents the value of its density. The optimization results are depicted in Fig. 10.

The post-processing results of the optimized B-spline hyper-surface shown in Fig. 10(a) are exhibited in Fig. 11. Unlike the 3D B-spline surface, the 4D B-spline hyper-surfaces cannot be operated directly in CAD software. Consequently, an operation of interpolating the threshold value points based on the uniformly sampled points is required. Theoretically, with enough sampled points, we can form the boundary of the 3D CAD model based on the threshold value points without errors. The interpolation operation can be implemented in Matlab (Natick, MA). As shown in Fig. 11(a), the result is a triangular patch model stored in Standard Tessellation Language (STL) format. Since the B-spline hyper-surface is smooth and continuous, the quality of the triangular patches derived from it is high, and the boundary is thus smooth and continuous. Unlike the triangular patch model derived from the element-based model, no additional boundary smoothing operation is required here. However, the triangular patch model lacks control parameters and the

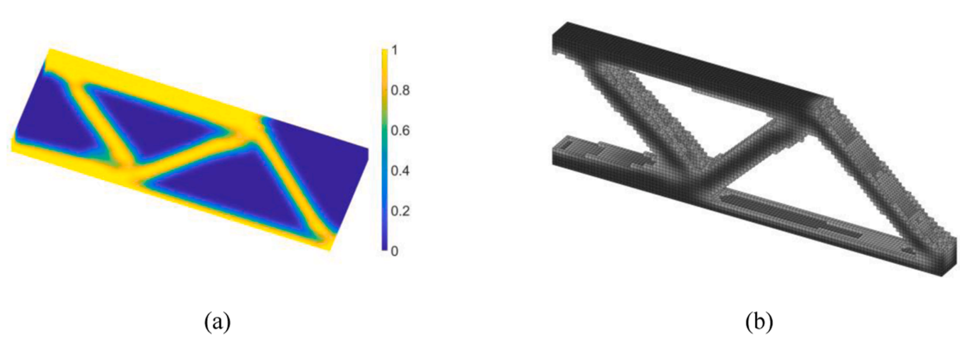

Fig. 10. Optimization results for the 3D cantilever of MTOBS: (a) B-spline hyper-surface (represented by uniformly sampled points), (b) density mesh distribution.

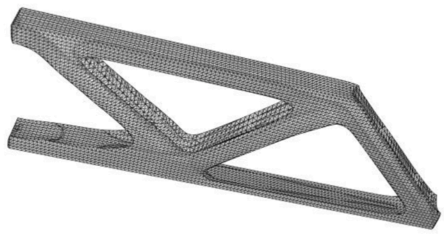

(a)

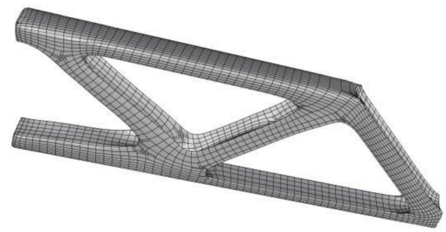

(b)

Fig. 11. The post-processing results of the optimized B-spline hyper-surface: (a) a triangular patch model by interpolating the threshold value points based on the uniformly sampled points, and (b) a NURBS patch model by fitting the boundary with a set of NURBS patches.

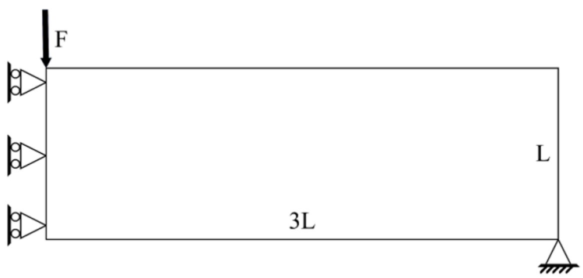

Fig. 12. A 2D HMBB beam diagram.

boundary cannot be edited directly in CAD software. We need to further employ a set of NURBS patches to fit the boundary of the triangular patch model by minimizing the distance between the NURBS patches and the triangular patches [73] and the result is shown in Fig. 11(b). The boundary of the fitted NURBS patch model can be edited by adjusting its control points and stored as a new igs file. A 3D cantilever's integrated process from MTOBS to an editable CAD model has been finished through the above operation.

5. Numerical examples

In this section, we choose three benchmark numerical examples of TO, including a 2D half Messerschmitt-Bölkow-Blohm (HMBB) beam, a 3D bridge, and a 3D compliant mechanism, to validate the performance of MTOBS in terms of computational efficiency and post-processing. Some related explorations and discussions of MTOBS are performed as well. Furthermore, the traditional SIMP method using B-spline to represent the density field [36], referred by "SIMP-B" in the following text for simplicity, is used for comparison. To compare fairly, the parameters of the MTOBS and SIMP-B are set consistently except for the analysis mesh.

The B-spline degrees in all directions are the same unless otherwise noted. The design domain coincides with the area of the corresponding effective knot spans. For simplicity, all the quantities are dimensionless. The Young's modulus is 1.0, and the minimum Young's modulus is 10^{-9}, while the Poisson's ratio is set to 0.3. The termination criterion for the iterations is that the sum of the compliances of the last 1–5 loops changes by less than a small positive value (e.g., 10^{-5}) compared to the sum of the last 6–10 loops. The post-processing procedure from the optimized B-spline surface/hyper-surface to the CAD model is skipped. All computations are performed on a PC with an AMD Ryzen 5 5600 G 3.90 GHz CPU and 16GB RAM.

5.1. 2D HMBB beam

This example investigates three issues: computational efficiency, filtering parameters, and optimization strategy. As a 2D HMBB beam shown in Fig. 12, the left edge is constrained horizontally, and the lower right corner is fixed. A unit point load is applied downward at the point of the top left corner. The objective is to minimize compliance with a volume fraction of 50%.

Table 1
Optimization results for the 2D HMBB beam: data comparison.

Items	MTOBS	SIMP-B
Compliance	207.57	207.50
Iteration number	93	104
Computational time(s)	7.43	26.25
Computational time per iteration (s)	0.08	0.25

5.1.1. Efficiency comparison between MTOBS and SIMP-B

The B-spline degree p is set to 2. The size of control points and effective knot spans are 152×52 and 150×50, respectively. A density mesh size of 300×100 and an analysis mesh size of 75×25 are assigned to discretize the design domain in MTOBS. To emphasize the efficiency of MTOBS, we compared the time taken by MTOBS and SIMP-B to generate a result of the same resolution. In SIMP-B, the analysis mesh and the density mesh share the same size, which is set to 300×100.The sensitivity filter radius is 2.0 times the size of a knot span. The value of the termination criterion for iterations is set to 10^{-5}. The optimization results are depicted in Table 1 and Fig. 13.

As expected, MTOBS can effectively reduce the computational cost by 68.00% on the total computational time and 71.70% on the computational time per iteration compared to SIMP-B. The post-processed CAD models obtained from the two methods are similar, and the compliance of MTOBS is only increased by 0.03%, demonstrating that MTOBS will not sacrifice the accuracy of optimization.

5.1.2. Effect of filtering parameters

Furthermore, in pursuit of a further understanding of the effect of the three filtering parameters mentioned in Section 3.3 on MTOBS, we continue to employ the 2D HMBB beam for investigation. The design domain is discretized by using a density mesh size of 300×100 and an analysis mesh size of 75×25. The value of the termination criterion for iterations is set to 10^{-5}. Three figures (i.e., Fig. 14, Fig. 15, and Fig. 16) depict the effect of B-spline degree p, sensitivity filter radius $r_{\min}$, and effective knot spans size D on the optimization results, respectively. Only the post-processed CAD models and the computational time per iteration t are displayed.

As shown in Fig. 14, increasing the B-spline degree causes a slight expansion of the filtering range. Conversely, the computational time per iteration increases significantly, even exceeding the time required by SIMP-B of degree $p = 2$. Thus, to ensure computational efficiency, the lower degree B-spline is adopted as much as possible to satisfy the requirement of the ideal configuration.

When using the low degree (e.g., $p = 2$) B-spine and not considering the sensitivity filter (i.e., $r_{\min}$=1.0), the post-processed CAD model boundary is inferior in smoothness, as shown in Fig. 15(a). Nevertheless,

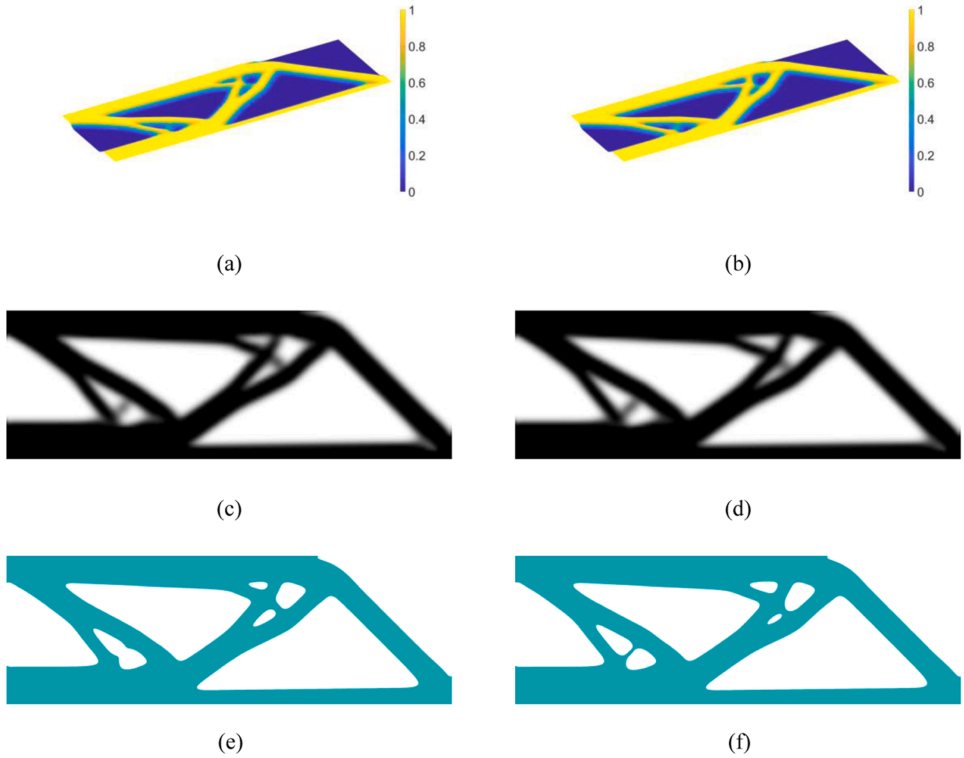

Fig. 13. Optimization results for the 2D HMBB beam: (a) B-spline surface (MTOBS), (b) B-spline surface (SIMP-B), (c) density mesh distribution (MTOBS), (d) density mesh distribution (SIMP-B), (e) post-processed CAD model (MTOBS), (f) post-processed CAD model (SIMP-B).

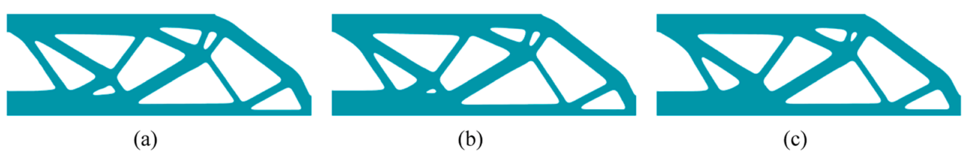

Fig. 14. Effect of B-spline degree, $D = 150 \times 50$, $r_{\min}$=1.5: (a) $p = 3$, $t = 0.17$ s, (b) $p = 6$, $t = 0.66$ s, (c) $p = 9$, $t = 1.24$ s.

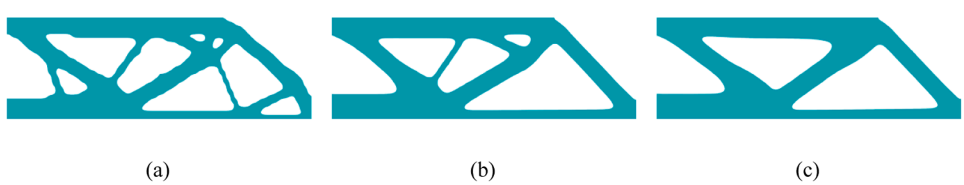

Fig. 15. Effect of sensitivity radius, $D = 75 \times 25$, $p = 2$: (a) $r_{\min}$=1.0, $t = 0.10$ s, (b) $r_{\min}$=1.1, $t = 0.10$ s, (c) $r_{\min}$=1.2, $t = 0.10$ s.

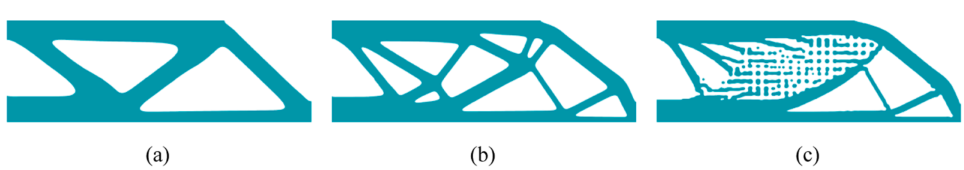

Fig. 16. Effect of effective knot spans size, $p = 2$, $r_{\min}$=1.5: (a) $D = 75 \times 25$, $t = 0.10$ s, (b) $D = 150 \times 50$, $t = 0.10$ s, (c) $D = 300 \times 100$, $t = 0.11$ s.

combined with Fig. 15(b) and Fig. 15(c), it can be found that the sensitivity filter can tackle the above issue and that increasing the filter radius yields a larger minimum feature length. In addition, the computational cost of sensitivity filter filtering once can be negligible compared with the time consumed in an iteration cycle.

Increasing the number of knot spans can help us obtain a smaller minimal feature length while using the sensitivity filter. According to the properties of the B-spline, when the number of knot spans increases in a specific region, the number of control points increases accordingly, to which the influence range of each control point in the region reduces, bringing about a smaller implicit filtering range. Fig. 16 demonstrates that increasing the number of effective knot spans leads to a smaller filtering range and minimal feature length while having almost no effect on the computational time per iteration. Combining the above

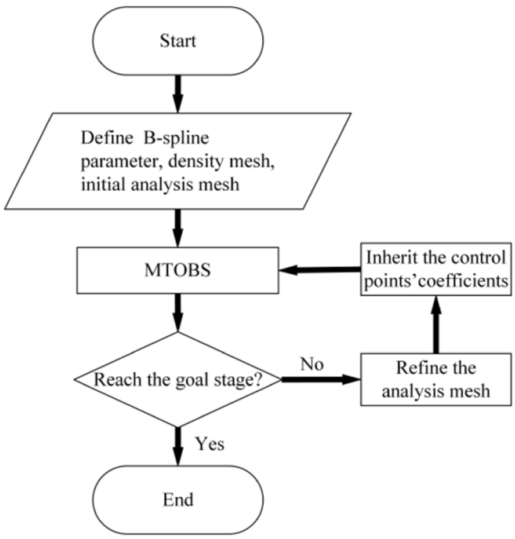

Fig. 17. The flowchart of the MAM optimization strategy.

discussion of the effects of the other two filtering parameters, it is recommended to adjust the sensitivity filtering radius and the number of knot spans to adjust the filtering range while using a lower degree B-spline.

5.1.3. A multiple analysis mesh optimization strategy

When the filtering range is not large enough, as shown in Fig. 16(c), the numerical artifacts of material discontinuities (i.e., QR-patterns) cannot be suppressed. Although increasing the filtering range can sufficiently suppress the QR-patterns, it will also increase the feature length. In order to obtain a smaller minimal feature length while suppressing the QR-patterns simultaneously, we propose a multiple analysis mesh (MAM) optimization strategy. The main idea is to divide the optimization process into several stages, each containing one complete MTOBS. The analysis mesh is refined stage by stage while the other parameters remain unchanged. Except for the initial stage, the control point coefficients of other stages are inherited from the previous stage. Fig. 17 further illustrates the flowchart of the proposed MAM.

We use the 2D HMBB beam to preliminary investigate MAM. The number of stages is set to 3, and the parameters in Fig. 16(c) are used in the initial stage. The analysis mesh sizes in the three stages are set to 75 $\times$ 25, 150 $\times$ 50, and 300 $\times$ 100 respectively. The analysis mesh size of the last stage is the same as the density mesh size, and the optimization effect is equivalent to SIMP-B. The first two stages adopt a relaxed termination criterion of iterations, which is 10^{-3}, and the last stage adopts 10^{-4}. Fig. 18 exhibits the optimization results, where I is the iteration number of each stage, and t is the corresponding computational time. For comparison, we directly perform SIMP-B using the parameters of the third stage and adopt the termination criterion of 10^{-4}. The results are shown in Fig. 19.

Compared with SIMP-B, a post-processed structure with a smaller minimal feature length is obtained through MAM, and the compliance is similar. In terms of efficiency, due to the preparation of the first two stages, the most time-consuming final stage requires fewer iterations. Consequently, the total computational time of MAM is still less than that of SIMP-B. It can be concluded that MAM suppresses the QR-patterns while keeping a small minimal feature length and has both accuracy and efficiency.

5.2. 3D bridge

A 3D bridge algorithm, shown in Fig. 20, is utilized to validate the performance of MTOBS. The intermediate flat layer with a thickness of $L/12$ is assumed to be a non-designable domain, and a uniform downward load is applied to the top face of the domain. The B-spline degree p is set to 2. The sizes of control points and effective knot spans are set to 98 $\times$ 26 $\times$ 10 and 96 $\times$ 24 $\times$ 8, respectively. Additionally, the density mesh is divided to 192 $\times$ 48 $\times$ 16.

The objective is to minimize compliance with a volume fraction of 20%. The analysis meshes are set as 48 $\times$ 12 $\times$ 4 and 192 $\times$ 48 $\times$ 16 respectively under the MTOBS and SIMP-B, and the value of the termination criterion for iterations is set to 10^{-4}. The optimization results are depicted in Table 2 and Fig. 21.

The results indicate that the MTOBS method under 3D design is also applicable to obtain optimized structures with reasonable material distribution and a well-defined layout, which further proves the feasibility of the design method. Similar to the 2D design, although the compliance of MTOBS is increased by 0.75%, the total computational time is reduced by 98.88%, and the computational time per iteration is reduced by 98.61%.

Fig. 19. Optimization result of SIMP-B: $I = 170$, $t = 52.50$ s, $c = 192.09$.

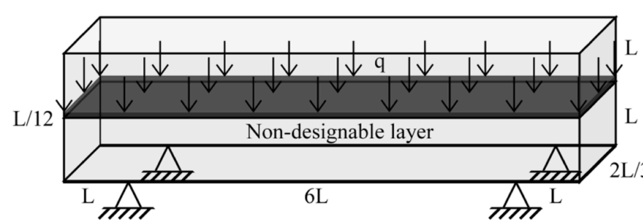

Fig. 20. A 3D bridge diagram.

Table 2
Optimization results for the 3D bridge: data comparison.

Items	MTOBS	SIMP-B
Compliance	5,775,626.38	5,414,611.18
Iteration number	84	104
Computational time(s)	124.66	11,082.93
Computational time per iteration (s)	1.48	106.57

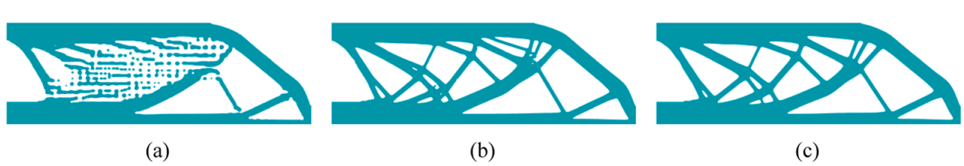

Fig. 18. Optimization results of the MAM optimization strategy: (a) the initial output results of state 1: $I = 92$, $t = 9.55$ s, (b) the intermediate output results of state 2: $I = 32$, $t = 4.26$ s, (c) the final output results of state 3: $I = 76$, $t = 21.69$ s, $c = 191.60$.

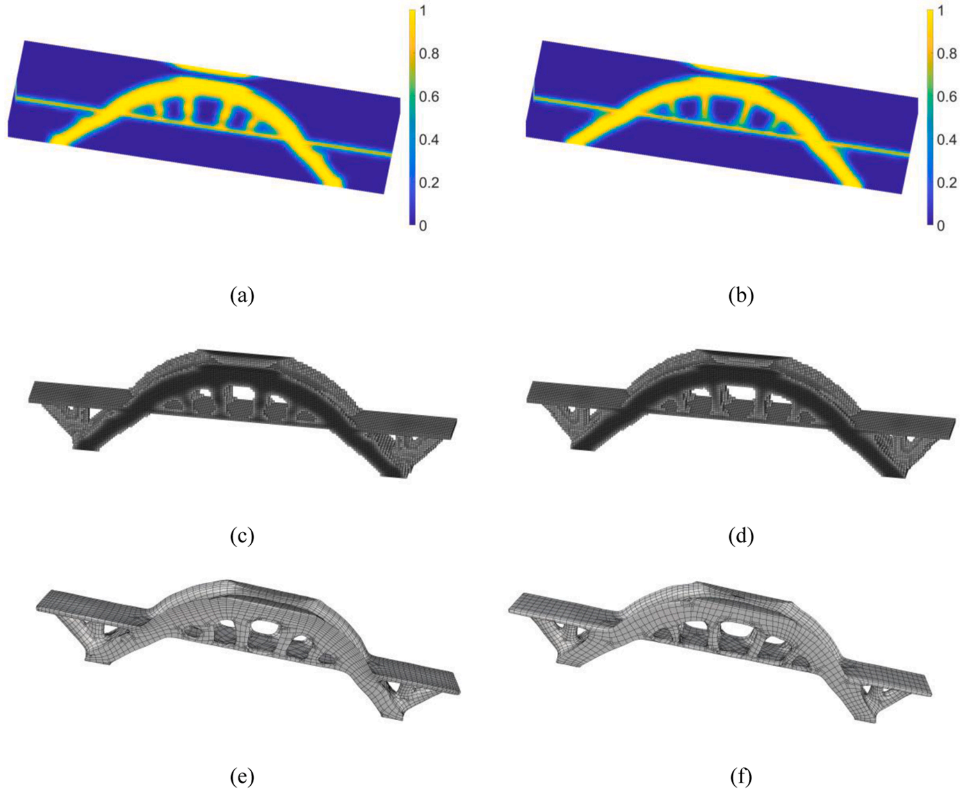

Fig. 21. Optimization results for the 3D bridge: (a) B-spline hyper-surface (MTOBS), (b) B-spline hyper-surface (SIMP-B), (c) density mesh distribution (MTOBS), (d) density mesh distribution (SIMP-B), (e) post-processed CAD model (MTOBS), (f) post-processed CAD model (SIMP-B).

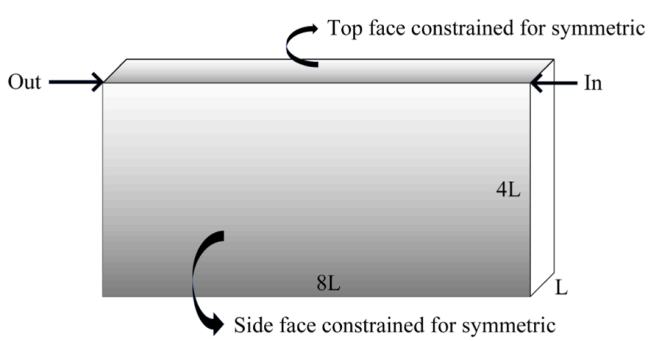

Fig. 22. A 3D force inverter diagram.

5.3. 3D compliant mechanism

A compliant mechanism is a structure that converts force or displacement through the deformation of flexible parts [74]. The design of benchmark compliant force/displacement inverters are often conducted in many studies to demonstrate the validity of the methods for topology optimization [75]. To further explore the applicability of the MTOBS method, a case of a 3D force inverter of compliant mechanism [76] is discussed. As shown in Fig. 22, the 3D force inverter has an input load and a dummy output load. The top and side face nodes can only move in the plane they are in. Furthermore, the external springs with a stiffness of 0.1 are added at the input and output ends. The objective of the optimization is to maximize the negative horizontal output displacement, and the volume fraction is 30%. The B-spline degree p is set to 2. The sizes of control points, effective knot spans, and the density mesh are set to $82 \times 42 \times 12$, $80 \times 40 \times 10$, and $160 \times 80 \times 20$, respectively. The value of the termination criterion for iterations is set to 10^{-4}. The optimization results when the analysis meshes are classified as $40 \times 20 \times 5$ and $160 \times 80 \times 20$ respectively under the MTOBS and SIMP-B method are depicted in Table 3 and Fig. 23.

Table 3
Optimization results for the 3D force inverter: data comparison.

Items	MTOBS	SIMP-B
Objective (displacement)	−1.8435	−1.9034
Iteration number	78	76
Computational time(s)	383.45	13,001.04
Computational time per iteration (s)	4.92	171.07

It can be revealed that the MTOBS method has excellent applicability for the 3D compliant mechanism. Furthermore, the difference of objective under the MTOBS method is not significant compared with SIMP-B, and the computational cost is considerably reduced, proving the superior performance advantage of MTOBS. In the design result depicted in Fig. 23, a thin structural connection, referred to as a hinge, can be observed. In fact, the hinge is theoretically reasonable because the ideal design is a rigid body linkage with rotating joints, which can generate large deformations and has zero strain energy [77]. However, hinge-based designs are controversial due to manufacturing difficulties and stress concentration, especially in micro-mechanical systems [78]. Hence, compliant mechanisms without hinges are preferable for most engineering applications. The filters and the stress constraints are commonly used to obtain the hinge-free compliant mechanism.

6. Conclusions

In this paper, we propose a promising method called multi-resolution topology optimization using B-spline (MTOBS). Numerical examples demonstrate that the proposed method is feasible and has great applicability to different design situations. Compared with the traditional SIMP method using B-spline (SIMP-B), the MTOBS significantly

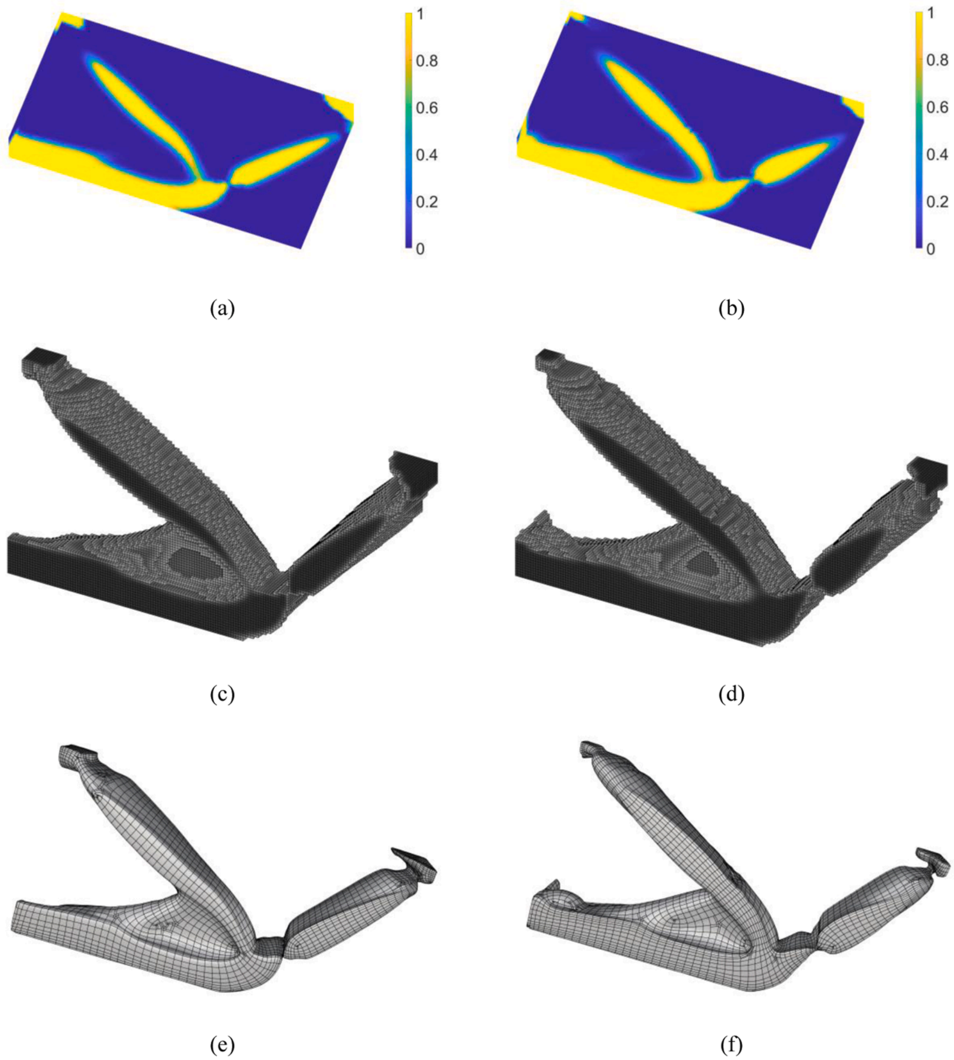

Fig. 23. Optimization results for the 3D force inverter: (a) B-spline hyper-surface (MTOBS), (b) B-spline hyper-surface (SIMP-B), (c) density mesh distribution (MTOBS), (d) density mesh distribution (SIMP-B), (e) post-processed CAD model (MTOBS), (f) post-processed CAD model (SIMP-B).

economizes the computational cost without affecting the structural performance. Besides, utilizing B-splines simplifies the post-processing process and thus facilitates the integrated process from optimization to design.

Moreover, the sensitivity filter circumvents the limitation of the inherent filtering effect brought by B-splines and improves the smoothness of the results, eliminating the need for manual detailing and benefits subsequent simulation and manufacturing. Some explorations and discussions on filtering parameters are carried out, and a MAM optimization strategy is proposed to solve the QR-patterns caused by insufficient filtering range without increasing the minimal feature length.

However, the proposed method is inadequate in dealing with the problems with irregular design domains. In future studies, U-spline [79], T-spline [80], and embedded domain method [81,82] will be exploited to tackle the above issues. Furthermore, MTOBS is also expected to be extended to other important TO methods and to combine with other efficient algorithms, such as CPU/GPU parallel computing, to further improve efficiency.

CRediT authorship contribution statement

Zhenbiao Guo: Conceptualization, Methodology, Software, Validation, Writing – original draft. **Hailiang Su:** Methodology, Validation. **Xinqing Li:** Writing – review & editing. **Yingjun Wang:** Conceptualization, Methodology, Supervision, Writing – review & editing.

Declaration of Competing Interest

The authors declare that they have no known competing financial interests or personal relationships that could have appeared to influence the work reported in this paper.

Data availability

Data will be made available on request.

Acknowledgment

This work has been supported by National Natural Science Foundation of China [No. 52075184], Guangxi Science and Technology Plan and Project [No. 2021AC19131], Open-funding Project of State Key Laboratory of Digital Manufacturing Equipment and Technology (Huazhong University of Science and Technology) [No.

DMETKF2021020]. These supports are gratefully acknowledged.

References

[1] Lindgaard E, Dahl J. On compliance and buckling objective functions in topology optimization of snap-through problems. Struct Multidiscip Optim 2013;47:409–21. https://doi.org/10.1007/s00158-012-0832-2.

[2] Madah H, Amir O. Truss optimization with buckling considerations using geometrically nonlinear beam modeling. Comput Struct 2017;192:233–47. https://doi.org/10.1016/j.compstruc.2017.07.023.

[3] Gonçalves M, Andrade-Campos A, Barroqueiro B. On the design of mechanical heterogeneous specimens using multilevel topology optimization. Adv Eng Softw 2023;175:103314. https://doi.org/10.1016/j.advengsoft.2022.103314.

[4] Gersborg-Hansen A, Sigmund O, Haber RB. Topology optimization of channel flow problems. Struct Multidiscip Optim 2005;30:181–92. https://doi.org/10.1007/s00158-004-0508-7.

[5] Nørgaard S, Sigmund O, Lazarov B. Topology optimization of unsteady flow problems using the lattice Boltzmann method. J Comput Phys 2016;307:291–307. https://doi.org/10.1016/j.jcp.2015.12.023.

[6] Gersborg-Hansen A, Bendsøe MP, Sigmund O. Topology optimization of heat conduction problems using the finite volume method. Struct Multidiscip Optim 2006;31:251–9. https://doi.org/10.1007/s00158-005-0584-3.

[7] Dirker J, Meyer JP. Topology optimization for an internal heat-conduction cooling scheme in a square domain for high heat flux applications. J Heat Transfer 2013; 135. https://doi.org/10.1115/1.4024615.

[8] Zhang L, Zhao Q, Chen J. Reliability-based topology optimization of thermo-elastic structures with stress constraint. Mathematics 2022;10:1091. https://doi.org/10.3390/math10071091.

[9] Zhou S, Li W, Li Q. Level-set based topology optimization for electromagnetic dipole antenna design. J Comput Phys 2010;229:6915–30. https://doi.org/10.1016/j.jcp.2010.05.030.

[10] Di Cesare N, Chamoret D, Domaszewski M. Optimum topological design of negative permeability dielectric metamaterial using a new binary particle swarm algorithm. Adv Eng Software 2016;101:149–59. https://doi.org/10.1016/j.advengsoft.2015.10.011.

[11] Christiansen RE, Lazarov BS, Jensen JS, Sigmund O. Creating geometrically robust designs for highly sensitive problems using topology optimization. Struct Multidiscip Optim 2015;52:737–54. https://doi.org/10.1007/s00158-015-1265-5.

[12] Desai J, Faure A, Michailidis G, Parry G, Estevez R. Topology optimization in acoustics and elasto-acoustics via a level-set method. J Sound Vib 2018;420: 73–103. https://doi.org/10.1016/j.jsv.2018.01.032.

[13] Chi H, Ramos DL, Ramos AS, Paulino GH. On structural topology optimization considering material nonlinearity: plane strain versus plane stress solutions. Adv Eng Software 2019;131:217–31. https://doi.org/10.1016/j.advengsoft.2018.08.017.

[14] Ramos AS, Paulino GH. Convex topology optimization for hyperelastic trusses based on the ground-structure approach. Struct Multidiscip Optim 2015;51: 287–304. https://doi.org/10.1007/s00158-014-1147-2.

[15] Sigmund O, Torquato S. Design of materials with extreme thermal expansion using a three-phase topology optimization method. J Mech Phys Solids 1997;45: 1037–67. https://doi.org/10.1016/S0022-5096(96)00114-7.

[16] Stegmann J, Lund E. Discrete material optimization of general composite shell structures. Int J Numer Methods Eng 2005;62:2009–27. https://doi.org/10.1002/nme.1259.

[17] Chen J, Zhao Q, Zhang L. Multi-material topology optimization of thermo-elastic structures with stress constraint. Mathematics 2022;10:1216. https://doi.org/10.3390/math10081216.

[18] Xia L, Breitkopf P. Concurrent topology optimization design of material and structure within FE2 nonlinear multiscale analysis framework. Comput Methods Appl Mech Eng 2014;278:524–42. https://doi.org/10.1016/j.cma.2014.05.022.

[19] Sivapuram R, Dunning PD, Kim HA. Simultaneous material and structural optimization by multiscale topology optimization. Struct Multidiscip Optim 2016; 54:1267–81. https://doi.org/10.1007/s00158-016-1519-x.

[20] Wang Y, Xu H, Pasini D. Multiscale isogeometric topology optimization for lattice materials. Comput Methods Appl Mech Eng 2017;316:568–85. https://doi.org/10.1016/j.cma.2016.08.015.

[21] Bendsøe MP, Kikuchi N. Generating optimal topologies in structural design using a homogenization method. Comput Methods Appl Mech Eng 1988;71:197–224. https://doi.org/10.1016/0045-7825(88)90086-2.

[22] Bendsøe MP. Optimal shape design as a material distribution problem. Struct Optim 1989;1:193–202. https://doi.org/10.1007/BF01650949.

[23] Sigmund O. A 99 line topology optimization code written in Matlab. Struct Multidiscip Optim 2001;21:120–7. https://doi.org/10.1007/s001580050176.

[24] Xie YM, Steven GP. A simple evolutionary procedure for structural optimization. Comput Struct 1993;49:885–96. https://doi.org/10.1016/0045-7949(93)90035-C.

[25] Querin OM, Steven GP, Xie YM. Evolutionary structural optimisation (ESO) using a bidirectional algorithm. Eng Comput (Swansea) 1998;15:1031–48. https://doi.org/10.1108/02644409810244129.

[26] Sethian JA, Wiegmann A. Structural boundary design via level set and immersed interface methods. J Comput Phys 2000;163:489–528. https://doi.org/10.1006/jcph.2000.6581.

[27] Wang MY, Wang X, Guo D. A level set method for structural topology optimization. Comput Methods Appl Mech Eng 2003;192:227–46. https://doi.org/10.1016/S0045-7825(02)00559-5.

[28] Wang Y, Benson DJ. Isogeometric analysis for parameterized LSM-based structural topology optimization. Comput Mech 2016;57:19–35. https://doi.org/10.1007/s00466-015-1219-1.

[29] Guo X, Zhang W, Zhong W. Doing topology optimization explicitly and geometrically—a new moving morphable components based framework. J Appl Mech 2014;81. https://doi.org/10.1115/1.4027609.

[30] Zhang W, Yang W, Zhou J, Li D, Guo X. Structural topology optimization through explicit boundary evolution. J Appl Mech 2016;84. https://doi.org/10.1115/1.4034972.

[31] Subedi SC, Verma CS, Suresh K. A review of methods for the geometric post-processing of topology optimized models. J Comput Inf Sci Eng 2020;20. https://doi.org/10.1115/1.4047429.

[32] Eschenauer HA, Kobelev VV, Schumacher A. Bubble method for topology and shape optimization of structures. Struct Optim 1994;8:42–51. https://doi.org/10.1007/BF01742933.

[33] Seo Y-D, Kim H-J, Youn S-K. Isogeometric topology optimization using trimmed spline surfaces. Comput Methods Appl Mech Eng 2010;199:3270–96. https://doi.org/10.1016/j.cma.2010.06.033.

[34] Hassani B, Khanzadi M, Tavakkoli SM. An isogeometrical approach to structural topology optimization by optimality criteria. Struct Multidiscip Optim 2012;45: 223–33. https://doi.org/10.1007/s00158-011-0680-5.

[35] Gao J, Gao L, Luo Z, Li P. Isogeometric topology optimization for continuum structures using density distribution function. Int J Numer Methods Eng 2019;119: 991–1017. https://doi.org/10.1002/nme.6081.

[36] Qian X. Topology optimization in B-spline space. Comput Methods Appl Mech Eng 2013;265:15–35. https://doi.org/10.1016/j.cma.2013.06.001.

[37] Costa G, Montemurro M, Pailhès J. A 2D topology optimisation algorithm in NURBS framework with geometric constraints. Int J Mech Mater Des 2018;14: 669–96. https://doi.org/10.1007/s10999-017-9396-z.

[38] Costa G, Montemurro M, Pailhès J. NURBS hyper-surfaces for 3D topology optimization problems. Mech Adv Mater Struct 2021;28:665–84. https://doi.org/10.1080/15376494.2019.1582826.

[39] Bertolino G., Costa G., Montemurro M., Perry N., Pourroy F. A general surface reconstruction method for post-processing of topology optimisation results. 2019.

[40] Costa Jr JCA, Alves MK. Layout optimization with h-adaptivity of structures. Int J Numer Methods Eng 2003;58:83–102. https://doi.org/10.1002/nme.759.

[41] Stainko R. An adaptive multilevel approach to the minimal compliance problem in topology optimization. Commun Numer Methods Eng 2006;22:109–18. https://doi.org/10.1002/cnm.800.

[42] Liao Z, Zhang Y, Wang Y, Li W. A triple acceleration method for topology optimization. Struct Multidiscip Optim 2019;60:727–44. https://doi.org/10.1007/s00158-019-02234-6.

[43] Wang Y, Liao Z, Ye M, Zhang Y, Li W, Xia Z. An efficient isogeometric topology optimization using multilevel mesh, MGCG and local-update strategy. Adv Eng Softw 2020;139:102733. https://doi.org/10.1016/j.advengsoft.2019.102733.

[44] Wang Y, Zheng W, Zheng Y, Da D. A new three-level mesh method to accelerate the structural topology optimization. Appl Math Model 2022;109:374–400. https://doi.org/10.1016/j.apm.2022.05.012.

[45] Borrvall T, Petersson J. Large-scale topology optimization in 3D using parallel computing. Comput Methods Appl Mech Eng 2001;190:6201–29. https://doi.org/10.1016/S0045-7825(01)00216-X.

[46] Kim TS, Kim JE, Kim YY. Parallelized structural topology optimization for eigenvalue problems. Int J Solids Struct 2004;41:2623–41. https://doi.org/10.1016/j.ijsolstr.2003.11.027.

[47] Vemaganti K, Lawrence WE. Parallel methods for optimality criteria-based topology optimization. Comput Methods Appl Mech Eng 2005;194:3637–67. https://doi.org/10.1016/j.cma.2004.08.008.

[48] Aage N, Poulsen TH, Gersborg-Hansen A, Sigmund O. Topology optimization of large scale stokes flow problems. Struct Multidiscip Optim 2008;35:175–80. https://doi.org/10.1007/s00158-007-0128-0.

[49] Wang Y, Wang Q, Deng X, Xia Z, Yan J, Xu H. Graphics processing unit (GPU) accelerated fast multipole BEM with level-skip M2L for 3D elasticity problems. Adv Eng Softw 2015;82:105–18. https://doi.org/10.1016/j.advengsoft.2015.01.002.

[50] Xia Z, Wang Y, Wang Q, Mei C. GPU parallel strategy for parameterized LSM-based topology optimization using isogeometric analysis. Struct Multidiscip Optim 2017; 56:413–34. https://doi.org/10.1007/s00158-017-1672-x.

[51] Wang S, Ed Sturler, Paulino GH. Large-scale topology optimization using preconditioned Krylov subspace methods with recycling. Int J Numer Methods Eng 2007;69:2441–68. https://doi.org/10.1002/nme.1798.

[52] Amir O, Aage N, Lazarov BS. On multigrid-CG for efficient topology optimization. Struct Multidiscip Optim 2014;49:815–29. https://doi.org/10.1007/s00158-013-1015-5.

[53] Amir O, Bendsøe MP, Sigmund O. Approximate reanalysis in topology optimization. Int J Numer Methods Eng 2009;78:1474–91. https://doi.org/10.1002/nme.2536.

[54] Long K, Gu C, Wang X, Liu J, Du Y, Chen Z, et al. A novel minimum weight formulation of topology optimization implemented with reanalysis approach. Int J Numer Methods Eng 2019;120:567–79. https://doi.org/10.1002/nme.6148.

[55] Nguyen TH, Paulino GH, Song J, Le CH. A computational paradigm for multiresolution topology optimization (MTOP). Struct Multidiscip Optim 2010;41: 525–39. https://doi.org/10.1007/s00158-009-0443-8.

[56] Nguyen TH, Paulino GH, Song J, Le CH. Improving multiresolution topology optimization via multiple discretizations. Int J Numer Methods Eng 2012;92: 507–30. https://doi.org/10.1002/nme.4344.

[57] Liu C, Zhu Y, Sun Z, Li D, Du Z, Zhang W, et al. An efficient moving morphable component (MMC)-based approach for multi-resolution topology optimization.

Struct Multidiscip Optim 2018;58:2455–79. https://doi.org/10.1007/s00158-018-2114-0.
[58] Lieu QX, Lee J. A multi-resolution approach for multi-material topology optimization based on isogeometric analysis. Comput Methods Appl Mech Eng 2017;323:272–302. https://doi.org/10.1016/j.cma.2017.05.009.
[59] Park J, Zobaer T, Sutradhar A. A two-scale multi-resolution topologically optimized multi-material design of 3D printed craniofacial bone implants. Micromachines (Basel) 2021. https://doi.org/10.3390/mi12020101.
[60] Keshavarzzadeh V, Kirby RM, Narayan A. Parametric topology optimization with multiresolution finite element models. Int J Numer Methods Eng 2019;119:567–89. https://doi.org/10.1002/nme.6063.
[61] Ortigosa R, Martínez-Frutos J. Multi-resolution methods for the topology optimization of nonlinear electro-active polymers at large strains. Comput Mech 2021;68:271–93. https://doi.org/10.1007/s00466-021-02030-4.
[62] Gupta DK, Langelaar M, van Keulen F. QR-patterns: artefacts in multiresolution topology optimization. Struct Multidiscip Optim 2018;58:1335–50. https://doi.org/10.1007/s00158-018-2048-6.
[63] Nguyen TH, Le CH, Hajjar JF. Topology optimization using the p-version of the finite element method. Struct Multidiscip Optim 2017;56:571–86. https://doi.org/10.1007/s00158-017-1675-7.
[64] Groen JP, Langelaar M, Sigmund O, Ruess M. Higher-order multi-resolution topology optimization using the finite cell method. Int J Numer Methods Eng 2017;110:903–20. https://doi.org/10.1002/nme.5432.
[65] Gupta DK, van Keulen F, Langelaar M. Design and analysis adaptivity in multiresolution topology optimization. Int J Numer Methods Eng 2020;121:450–76. https://doi.org/10.1002/nme.6217.
[66] Mezzadri F, Qian X. Density gradient-based adaptive refinement of analysis mesh for efficient multiresolution topology optimization. Int J Numer Methods Eng 2022;123:465–504. https://doi.org/10.1002/nme.6863.
[67] Sigmund O. Design of material structures using topology optimization 1994.
[68] Sigmund O. On the design of compliant mechanisms using topology optimization. Mech Struct Mach 1997;25:493–524. https://doi.org/10.1080/08905459708945415.
[69] Sigmund O. Morphology-based black and white filters for topology optimization. Struct Multidiscip Optim 2007;33:401–24. https://doi.org/10.1007/s00158-006-0087-x.
[70] Piegl L., Tiller W. The NURBS book: springer science & business media; 1996.
[71] Feng S, Zhang W, Meng L, Xu Z, Chen L. Stiffener layout optimization of shell structures with B-spline parameterization method. Struct Multidiscip Optim 2021;63:2637–51. https://doi.org/10.1007/s00158-021-02873-8.
[72] Bendsøe MP. Optimization of structural topology, shape, and material. Springer; 1995.
[73] Floater MS. Parametrization and smooth approximation of surface triangulations. Comput Aided Geom Des 1997;14:231–50. https://doi.org/10.1016/S0167-8396(96)00031-3.
[74] Howell LL. Compliant mechanisms. In: McCarthy JM, (editor). 21st Century kinematics. London: Springer London; 2013. p. 189–216. https://doi.org/10.1007/978-1-4471-4510-3_7.
[75] Zhu B, Zhang X, Zhang H, Liang J, Zang H, Li H, et al. Design of compliant mechanisms using continuum topology optimization: a review. Mech Mach Theory 2020;143:103622. https://doi.org/10.1016/j.mechmachtheory.2019.103622.
[76] Liu K, Tovar A. An efficient 3D topology optimization code written in Matlab. Struct Multidiscip Optim 2014;50:1175–96. https://doi.org/10.1007/s00158-014-1107-x.
[77] Wang MY. A kinetoelastic formulation of compliant mechanism optimization. J Mech Robot 2009;1. https://doi.org/10.1115/1.3056476.
[78] Sardan O, Eichhorn V, Petersen DH, Fatikow S, Sigmund O, Bøggild P. Rapid prototyping of nanotube-based devices using topology-optimized microgrippers. Nanotechnology 2008;19:495503. https://doi.org/10.1088/0957-4484/19/49/495503.
[79] Thomas DC, Engvall L, Schmidt SK, Tew K, Scott MA. U-splines: splines over unstructured meshes. Comput Methods Appl Mech Eng 2022;401:115515. https://doi.org/10.1016/j.cma.2022.115515.
[80] Scott MA, Li X, Sederberg TW, Hughes TJR. Local refinement of analysis-suitable T-splines. Comput Methods Appl Mech Eng 2012;213-216:206–22. https://doi.org/10.1016/j.cma.2011.11.022.
[81] Wang Y, Gao L, Qu J, Xia Z, Deng X. Isogeometric analysis based on geometric reconstruction models. Front Mech Eng 2021;16:782–97. https://doi.org/10.1007/s11465-021-0648-0.
[82] Wang Y, Xiao M, Xia Z, Li P, Gao L. From computer-aided design (CAD) toward human-aided design (HAD): an isogeometric topology optimization approach. Engineering 2022. https://doi.org/10.1016/j.eng.2022.07.013.